A Systematic Method for the Calibration of FEA Model of Synchronous Reluctance Machines Considering Manufacturing Effects

A Systematic Method for the Calibration of FEA Model of Synchronous Reluctance Machines Considering Manufacturing Effects

ANDREA CREDO [1] (Member, IEEE) AND PAOLO PESCETTO [2] (Member, IEEE)

[1]Department of Industrial and Information Engineering and Economics, University of L'Aquila, 67100 L'Aquila, Italy
[2]Energy Department Galileo Ferraris, Politecnico di Torino, 10129 Torino, Italy

CORRESPONDING AUTHOR: ANDREA CREDO (e-mail: andrea.credo@univaq.it).

This work was supported by the European Union – NextGenerationEU, Mission 4, Component 1, under the Italian Ministry of University and Research (MUR) National Innovation Ecosystem grant ECS00000041 – VITALITY – CUP E13C22001060006.

ABSTRACT The recent advances in computational power and motor design software, supported by finite elements analysis (FEA), permit accurate prediction of the losses and electromagnetic performance of the machine at the design stage. Anyway, the simulation accuracy strictly depends on the real motor geometry and material properties, which are affected by the manufacturing process. This article offers a systematic method for accurately calibrating the electromagnetic FEA models, permitting to consider the production process within the motor design stage. A synchronous reluctance motor prototype is designed, manufactured, and experimentally characterized, and the measured flux and torque characteristics are exploited for ex-post calibrating the FEA model of the machine. This approach led to a reduction in torque estimation error from 18% to 4%, and an improvement of the flux maps evaluation, thus enhancing and validating the design procedure and permitting further optimization steps of machines with similar geometry and dimensions. The effects are particularly evident in the proposed motor due to the reduced size of the rotor flux barriers, stator teeth, and yoke. The mechanical tolerances are analyzed through a Monte Carlo analysis covering different areas of the machine. Then, the effects of uncertain airgap length and iron degradation due to the manufacturing process are considered, determining an equivalent degraded BH curve.

INDEX TERMS BH curve estimation, electric motor applications in vehicles, machine design, magnetic properties degradation, model calibration, Monte Carlo analysis, optimization, self-commissioning techniques, synchronous reluctance motor drive.

I. INTRODUCTION

Industrial electric motors, including blowers, fans, manufacturing machines, and pumps, consume up to 40% of the globally generated electrical energy [1], [2]. Remarkably, approximately 70% of industrial electricity is attributed to electric motor systems, making them a critical load type within the industry. Therefore, enhancing the efficiency of electric motors stands as a compelling strategy to mitigate energy consumption and reduce the associated environmental impact. Nowadays, 90% of the installed electric motors are three-phase squirrel-cage induction motors (IMs) [1], as they benefit of cost-effectiveness, robustness, and direct grid compatibility for single-speed operations. However, the efficiency of IMs is typically lower than that of synchronous reluctance (SynRel) motors, primarily because of the Joule losses in the rotor cage [3], [4].

The motor design process is typically based on geometry optimization, considering the machine's operation in a single working point [5]. However, synchronous machines are often applied in variable speed drives, and the operating cycle normally includes load and speed variations. Therefore, a finer optimization of the machine geometry can be achieved by considering different working points at the design stage [6], [7], [8], [9].

Nowadays, electrical machine simulation software based on finite element analysis (FEA) offer precise computation

of machine losses and performances in terms of average torque, torque ripple, flux linkage, and required voltage. An accurate machine analysis might require a fine simulation mesh, as well as a short simulation step-time, at least when the losses and torque ripple computation is included. Moreover, a postprocessing stage is often necessary for evaluating numerous aspects, such as the effect of the manufacturing process in terms of mechanical tolerances and BH curve degradation, possibly requiring considerable computational time [10]. However, said computational is reasonably reduced by the modern simulation software and the increasing computational power [11], [12].

Several studies have explored methods for assessing the impact of manufacturing tolerances on motor performance. Advanced techniques, such as Monte Carlo simulations and statistical tolerance analysis, have been proposed to manage large-scale uncertainties, particularly in nonuniform uncertainty method (non-UUM) scenarios [13]. These approaches are especially suitable for permanent magnet synchronous motors (PMSMs), which are more sensitive to manufacturing variations [14], [15]. While non-UUM methods tend to offer higher accuracy, they can be computationally intensive. To mitigate this, [13] suggests a modified analytical approach that identifies worst-case uncertainty combinations, thereby reducing the number of FEM calculations to only a few key cases. This streamlines the analysis while ensuring accuracy across various pole/slot configurations and magnet shapes. However, in this work, a UUM combined with Monte Carlo analysis was employed, given the robustness of SynRel motors and their tolerance to manufacturing variations.

Recent studies have introduced statistical models and tolerance-aware optimization strategies, particularly for PMSMs. Robust design strategies [16] integrate manufacturing deviations into the early-stage optimization process using noise-aware genetic algorithms and surrogate modeling techniques. Other state-of-the-art methods combine evolutionary algorithms, such as Non-dominated Sorting Genetic Algorithm (NSGA-II), Strength Pareto Evolutionary Algorithm (SPEA2), Particle Swarm Optimization (PSO), and Differential Evolution (DE), with surrogate modeling to reduce computational burden. While this allows for the exploration of multiobjective, constraint-rich, and highly nonlinear design spaces, robustness is often assessed only as a postprocessing step. Such approaches may neglect critical regions of the design space that offer better tradeoffs between nominal performance and tolerance sensitivity [17]. Other methods embed robustness directly into the optimization loop, but this dramatically increases the computational time. For this reason, strategies such as parameter sensitivity screening and probabilistic importance measures have been proposed to prioritize impactful tolerances while reducing the number of required FEA evaluations. In addition, Kolb and Hameyer [15], [18]; provided an in-depth sensitivity analysis of PMSMs using global design of experiments and magnetic FEA. They highlight that the combined influence of multiple manufacturing tolerances can cause significant deviations in torque, torque ripple, and acoustic behavior. Unlike traditional one-factor-at-a-time methods, the global sensitivity approach captures interdependencies and identifies the most influential tolerances, thereby guiding cost-effective adjustments.

Despite the relevance of these effects, most studies still focus on PMSMs and axial flux machines, leaving a gap in the modeling and calibration of SynRel motors under realistic manufacturing deviations in tolerances and magnetic properties variation of the degraded materials.

The impact of the manufacturing process on machine characteristics depends on several aspects. As an example, for laser cut laminations, the steel degradation and the thickness of the damaged area depend on the adopted laser technology and the process speed, and it is hardly estimated analytically [19]. Similar considerations apply to sheared laminations. Due to the impossibility of analytically determining these effects with accuracy, the FEA models are often corrected based on experience and experimental measures on a prototype. This process is often based on trial and error, resulting time-consuming and normally leading to a suboptimal calibration.

To solve this issue, this article proposes a systematic procedure to identify the effects of the manufacturing process and to include them in the motor design procedure. This includes mechanical tolerances and magnetic properties degradation due to laser cutting or shearing. The method is validated on a SynRel motor prototype, which has been experimentally characterized by measuring the dq-axes flux linkage saturation curves (also called flux maps), together with the current versus torque characteristic. This experimental stage permitted a better estimation of the magnetic properties of the material and a fine ex-post calibration of the FEA model of the machine. The obtained calibrated model is extremely useful for further geometry optimization, as well as for the design of new SynRel machines of similar size.

Therefore, the limitation of the proposed model is its applicability. The optimization can use the obtained model if the dimensions, the manufacturing process, and the material are similar to the ones used for the model realization. The rest of this article is organized as follows. The machine ratings and model are presented in Section II. Section III describes the experimental tests adopted for the torque, flux maps, and leakage inductance measurements. The core of this article is detailed in Section IV, discussing the proposed approach for model refinement. Section V provides the final remarks and Section VI concludes this article.

II. SYNCHRONOUS RELUCTANCE MOTOR

The SynRel motor is often adopted in industrial applications for its cost-effectiveness, competitive efficiency, and power density [20], although it exhibits a lower power factor if compared to permanent magnet synchronous machines and IMs counterparts [21]. The torque capability of the SynRel is closely linked to its magnetic anisotropy, achieved through careful optimization of the rotor shape. The increased rotor anisotropy also enables the implementation of

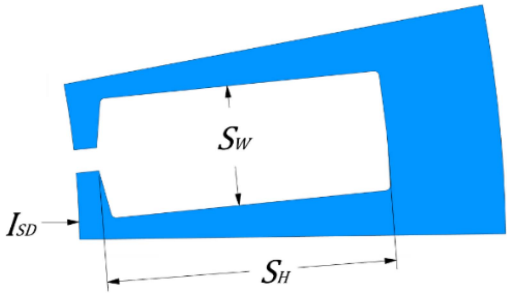

FIGURE 1. Stator slot and design variables.

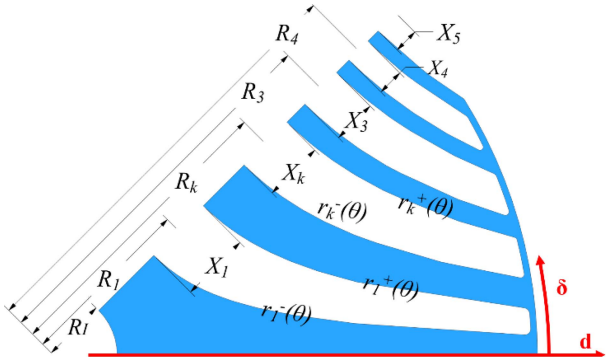

FIGURE 2. Fluid-shaped rotor barriers (half pole) and design variables.

saliency-based sensorless control algorithms, particularly effective at zero and low speeds [22], where the model-based approaches [23] would fail. In most applications, these sensorless algorithms necessitate knowledge of machine parameters, particularly the magnetic self- and cross-saturation characteristics, often obtained through self-commissioning techniques [24], [25].

A. MOTOR MODEL

The stator voltage equation can be written in the dq rotating reference frame

$$\boldsymbol{v_{dq}} = R_s \boldsymbol{i_{dq}} + \frac{d\boldsymbol{\lambda_{dq}}}{dt} + \boldsymbol{J}\omega\boldsymbol{\lambda_{dq}} \tag{1}$$

where $\boldsymbol{v_{dq}}$,$\boldsymbol{i_{dq}}$, and $\boldsymbol{\lambda_{dq}}$ are the voltage, current, and flux vectors, respectively; R_s is the stator resistance, and ω the electrical speed and $\boldsymbol{J} = \begin{bmatrix} 0 & -1 \\ 1 & 0 \end{bmatrix}$ is the imaginary unit matrix. The SynRel motors are often prone to severe magnetic saturation and cross-saturation, leading to a nonlinear magnetic model

$$\begin{cases} \lambda_d = \lambda_d \left(i_d, i_q\right) \\ \lambda_q = \lambda_q \left(i_d, i_q\right). \end{cases} \tag{2}$$

Being p the number of pole pairs, the electromagnetic torque T is obtained from the cross-product between the current and the flux vectors

$$T = \frac{3}{2} p \left(\lambda_d i_q - \lambda_q i_d\right). \tag{3}$$

B. PROTOTYPE DESIGN

The motor adopted in this work is a SynRel prototype specifically designed for optimal efficiency within a specific duty cycle [26]. The target application is a vehicle auxiliary system, specifically a cooling fan. This application requires variable speed and torque operation to ensure efficient thermal management across different operating conditions, such as during high cooling demand or standby phases. Figs. 1 and 2 illustrate the design variables employed in the optimization process of the stator and rotor respectively. In general, several geometries can be adopted for designing the rotor flux barriers of a SynRel machine, e.g., circular, linear, or fluid shape,

TABLE 1. Design Requirements and Measured Torque for the Four Operating Points

Operating Point	Speed (r/min)	Current (Apk)	Design torque (N·m)	Measured torque (N·m)
1	4000	65.5	2.26	2.11
2	6000	51.6	1.60	1.51
3	8000	32.5	0.86	0.69
4	8000	16.1	0.22	0.17

to maximize the average torque while minimizing its fluctuations. In this study, a fluid-shaped geometry was selected, targeting a significant reduction of the torque ripple [27], [28].

The geometry of fluid shape flux barriers is defined by the following:

$$r_i^{\pm}(\delta) = R_I \sqrt[p]{\frac{C_{(i)}^{\pm} + \sqrt{\left(C_{(i)}^{\pm}\right)^2 + 4\sin^2(p\delta)}}{2\sin(p\delta)}} \tag{4}$$

where R_I is the shaft radius, δ is the mechanical angle with respect to the d-axis, and $C_{(i)}^{\pm}$ is a parameter defined by the design variables. For the lower (–) and upper (+) lines of each barrier, $C_{(i)}^{\pm}$ is computed as follows:

$$C_{(i)}^{\pm}(X_i, R_i) = \frac{\left(\frac{R_i \pm X_i}{R_I}\right)^{2p} - 1}{\left(\frac{R_i \pm X_i}{R_I}\right)^{p}} \tag{5}$$

where i is the index of the flux barrier and R_i, X_i are indicated in Fig. 2.

This motor was designed to target the maximum efficiency over a specific load cycle, made of four operating points (OPs), reported in Table 1. In particular, OP 3 corresponds to rated torque and speed in S1 operation, OPs 1 and 2 represent two short-period overloads that must be maintained for a few minutes and OP4 is at nominal speed, partial load. The FEA model adopted for the motor design includes an accurate evaluation of iron loss, mechanical friction and windage.

Fig. 3 reports the motor geometry and the magnetic flux density computed at rated torque (OP3). The maximum magnetic flux density in the stator yoke and in the rotor carrier is close to the saturation knee of the adopted steel (1.45 T),

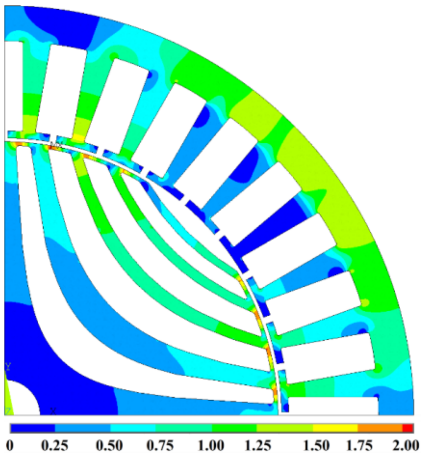

FIGURE 3. Geometry and flux density (T) of the designed SynRel motor (1 pole).

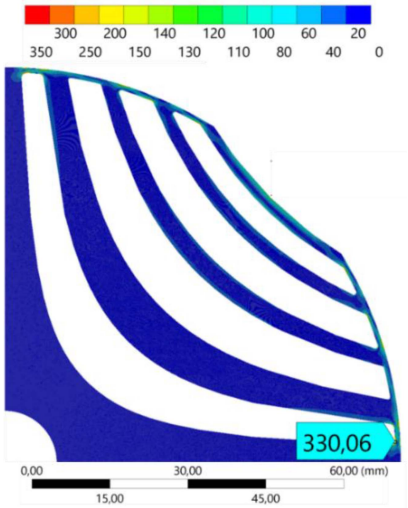

FIGURE 4. Equivalent Von-Mises stress at the maximum speed (8000 r/min).

to fully exploit the iron volume. The electromagnetic motor design is complemented by a mechanical analysis.

Fig. 4 depicts the Von-Mises stress on the machine at the rated speed (8000 r/min), coincident with the maximum required speed. The maximum stress is limited to 330 Mpa, with a reasonable safety margin with respect to the elastic limit of the material (460 Mpa).

C. PROTOTYPE MANUFACTURING

A prototype of the designed motor has been manufactured and tested. The stator and rotor cores have been laser cut. The final application requires hairpin windings. However, a round wire was used for the prototype, as the hairpin technology is inherently devoted to mass production, while only one sample was required for the design validation. Fig. 5 shows the manufactured prototype.

The main parameter and performance are reported in Table 2, where the subscript N stands for nominal values.

FIGURE 5. Manufactured SynRel prototype.

TABLE 2. Main Parameters and Performance

Variable	Value	Variable	Value
I_{SD}	77.2 mm	$T_{e,N}$	0.86 N·m
S_W	5.2 mm	R_S	24 mΩ
S_H	12.5 mm	$I_{d,N}$	16 A
$\lambda_{d,N}$	0.0115 Vs	$I_{q,N}$	32 A
$\lambda_{q,N}$	0.005 Vs	V_{DC}	48 V

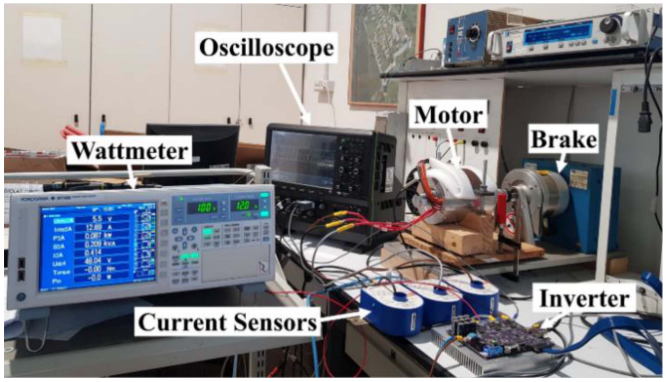

FIGURE 6. Experimental setup for prototype characterization.

III. PROTOTYPE CHARACTERIZATION

The core of this work is a systematic technique for ex-post correcting the FEA model based on the manufactured prototype. This permits a more accurate representation of the machine to be used for further design optimization.

With this goal, a series of experimental tests were executed to characterize the prototype. The setup, shown in Fig. 6, includes a dc power supply Xantrex XDC 60-100, a hysteresis dynamometer MAGTROL (HD-710-8NA-0040) as brake and torque transducer, three LEM current sensors, a Yokogawa WT 1800 wattmeter for the electric power measurement (dc and ac power) and a custom-designed inverter.

A. STEADY-STATE TORQUE ON THE MTPA

First, the machine was tested in the four operating points considered for the machine design, with the motor current controlled on the MTPA locus. The measured torque is reported in Table 2 and compared with the FEA results.

As can be seen, the experimental results are below the FEA expectations in the two overload points (OP1 and OP2), resulting in a torque discrepancy of –6.6% and –5.6%, respectively, for equal current. An even more significant torque discrepancy is found in OP3 and OP4 (–14.7% and –22.7%, respectively). A current of 36 Apk was required for experimentally obtaining the nominal torque, i.e., ≈20% higher thant the design current. This behavior indicates that the model is particularily inaccurate at at partial load, i.e., with the motor operating in the linear part of the magnetic saturation curve. The accuracy is higher in the saturation region, but still with a relevant discrepancy. This can be explained considering that the manufacturing process highly affects the linear part of the magnetization curve, while its influence is lower in the saturation region. More details can be found in Section IV.

B. FLUX MAPS MEASUREMENT

As described in (2), due to the severe magnetic saturation, the SynRel machines are characterized by highly nonlinear current-to-flux relationships, also called flux maps. The flux maps include several phenomena that FEA hardly models. First, the adopted FEA model is a two-dimensional (2-D) representation of the machine. This permits a computationally efficient simulation that can be handled in optimization algorithms, but the end-winding contribution to the leakage fluxes is hardly evaluated. Second, iron self- and cross-saturation depend on the real B–H saturation curve, which may differ from the ratings declared in the steel datasheet due to several effects, including iron degradation in the manufacturing process. This is particularly critical in the structural ribs area, which strongly influences the electromagnetic performance of the machine, and it is deeply affected by mechanical tolerances and manufacturing effects, such as laser cutting or lamination blanking. Therefore, an accurate experimental measurement of the flux maps is crucial for ex-post calibrating the FEA model.

To this goal, the self-saturation characteristics of the $d-$ and q-axes were measured on the prototype under test and compared with the FEA results. The standstill method described in [18] was adopted, which was demonstrated to be compatible with the state-of-the-art procedures for measuring flux maps. Moreover, this method proved to be accurate in commercial motors of different sizes and insensitive to motor resistance estimation or inverter voltage drop compensation.

The flux maps identification procedure is composed of 2 tests. Test #1 is adopted for measuring the d-axis saturation characteristic $\lambda_d(i_d, i_q = 0)$. The d-axis is excited with a hysteresis-controlled square wave voltage whose polarity is reversed any time the absolute value of the current component $|i_d|$ overcomes a defined threshold value $i_{d,\max}$. Meanwhile,

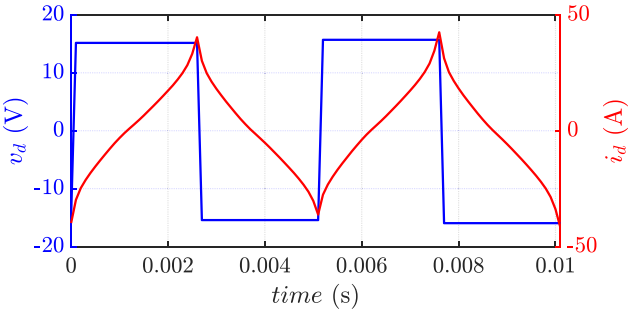

FIGURE 7. Voltage reference and measured current during experimental measurement of $\lambda_d(i_d)$ characteristic.

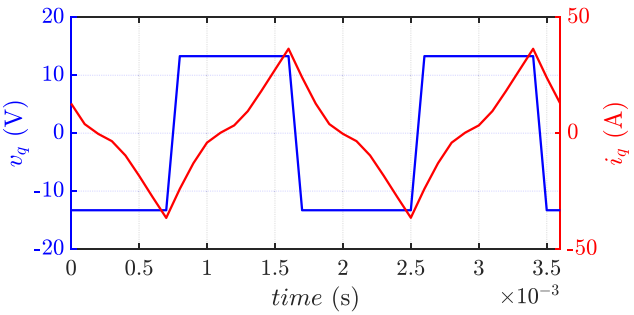

FIGURE 8. Voltage reference and measured current during experimental measurement of $\lambda_q(i_q)$ characteristic.

the q-axis current i_q is closed-loop controlled to zero. The corresponding control block diagram is reported in [24]. The d-axis flux is computed by open-loop integration of the machine EMF in the discrete-time domain

$$\lambda_d(k) = \lambda_d(k-1) + T_s \cdot \left(v_d^*(k-2) - R_s i_d(k-1)\right) \quad (6)$$

where T_s is the PWM period, equal to the sampling time.

The second step of the procedure, i.e., test #2, is dual to the first one, but the q-axis is excited to measure the $\lambda_q(i_q, i_d = 0)$ saturation curve. The q-axis is hysteresis controlled with a square wave voltage reversed when $|i_q|$ overcomes a threshold value $i_{q,\max}$, while $i_d = 0$ is closed-loop imposed. The λ_q self-saturation characteristic is determined as follows:

$$\lambda_q(k) = \lambda_q(k-1) + T_s \cdot \left(v_q^*(k-2) - R_s i_q(k-1)\right) \quad . \quad (7)$$

The current and flux waveforms for the two tests are reported in Figs. 7 and 8 for the $d-$ and q-axes, respectively, and the corresponding saturation curves are shown in Fig. 9.

The comparison between the measured flux maps and the FEA model, reported in Fig. 9, highlighted a decent accuracy of the simulated q-axis flux linkage, while a relevant deviation is observed for the d-axis, with an overestimation of the flux curve in the linear region. This confirms that the manufacturing process mostly affects the motor performance at partial load rather than in the saturation region.

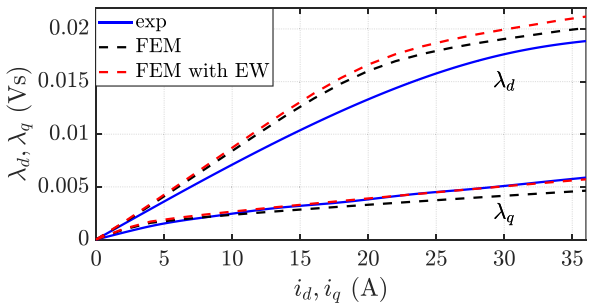

FIGURE 9. Comparison of $\lambda_d(i_d)$ and $\lambda_q(i_q)$ characteristics; blue: experimental results, dashed black: base FEA model, dashed red: base FEA with EW adjustment.

C. LEAKAGE INDUCTANCE AND END-WINDING EFFECTS

The leakage inductance was determined to accurately account for the effects of slot and end-winding (EW) leakage flux in the 2-D FEA simulation. First, the slot leakage inductance was estimated using a 2-D FEA simulation of the stator, excited with ac current at various frequencies, while excluding the rotor model. Next, the end-winding contribution was evaluated via a 3-D FEA simulation, again considering only the stator without the rotor. The EW leakage inductance was derived as the difference between the total leakage inductance obtained from the 3-D and 2-D FEA simulations.

Subsequently, the total leakage inductance, incorporating both EW and slot effects, was experimentally determined by measuring the stator inductance without the rotor core. The measurements were conducted using a precision LCR meter (Keysight E4980AL) across a broad frequency range, including the maximum motor speed. Despite this extensive range, no significant variation in leakage inductance was observed. The measured total leakage inductance (35 μH) was found to be in good agreement with the value predicted by the FEA simulations.

Finally, the EW leakage inductance was incorporated into each phase of the 2-D FEA model. The newly computed flux saturation curves are reported in red in reported in Fig. 9. As can be seen, the inclusion of EW effects permits to perfectly match the $\lambda_q(i_q)$ curve, while further investigation is needed for the d-axis.

D. MECHANICAL LOSS AND INERTIA

The mechanical losses were calculated based on the bearings datasheet and further validated through deceleration (coast-down) tests conducted at different speeds. These tests enabled an accurate estimation of the mechanical losses and machine's inertia, ensuring a reliable basis for comparing FE simulations with experimental results.

IV. EX-POST CALIBRATION OF THE FEA MODEL

The differences between the experimental results and the FEA model can be due to the following two main sources of uncertainty.

1) The design geometry and the prototype differ due to the mechanical tolerances. In this respect, the most critical parameter possibly affected by mechanical tolerance is the airgap thickness, and it will be treated separately.
2) A difference in the electromagnetic properties of the iron, which is degraded by the manufacturing process.

To evaluate the accuracy of the FEA model w.r.t. the measurements, two variables were considered, i.e., the torque and d-axis flux at the nominal operating conditions (OP3).

A. EFFECT OF MANUFACTURING TOLERANCES

The manufacturer declared a maximum mechanical tolerance of ± 0.05 mm. This tolerance was verified using a coordinate measuring machine, that evaluated every critical geometrical parameter influencing the machine's performance. This includes stator and rotor geometries. The inner and outer stator diameters and their difference, i.e., the airgap length, were verified as well. Similarly, the stator slot dimensions, rotor barrier dimensions and positions, and rotor radial ribs were verified, all adhering to the specified tolerance of ± 0.05 mm. Measurements made on a single lamination revealed a maximum deviation of 0.025 mm from the design specifications.

These verified dimensions provide a solid basis for evaluating the impact of manufacturing tolerances through Monte Carlo simulations [10], simultaneously varying several design parameters. Considering a normal distribution of each geometrical dimension, the analysis is repeated on varying all the design variables within the assigned distribution. By creating a reasonable number of sample machines, it is possible to evaluate the output distribution. A normal distribution is assigned to all the design variables, with the mean value determined by the nominal design and a standard deviation of one-third of the declared tolerance. A UUM approach was employed, which is sufficient given the robust performance of SynRel machines with respect to manufacturing tolerances.

The computed torque is normalized respect to its nominal value and reported in the bar graph in Fig. 10, where the y-axis represents the probability density as a function of simulated torque. The probability density of the torque was analytically fitted, assuming again a normal distribution. The fitted curve, reported in Fig. 10, presents a mean value of 0.856 N·m (0.995 p.u.), close to the rated one (0.86 N·m), and a standard deviation of 0.004 N·m (0.047 p.u.).

It should be highlighted that the Monte Carlo analysis is performed on a 2-D FEA representation of the machine. This corresponds to assuming that every lamination is equally affected by the manufacturing tolerances. In practice, every lamination might present a different mechanical tolerance. This effect would further reduce the standard deviation in the torque distribution. If the machine is assembled with a batch of N different laminations (in this case $N = 120$), the distribution of the motor torque changes, as represented in Fig. 11. In particular, the distribution maintains a normal behavior with the same mean value, but the standard deviation is strongly reduced, with a ratio approximately equal to $\sqrt{N}$.

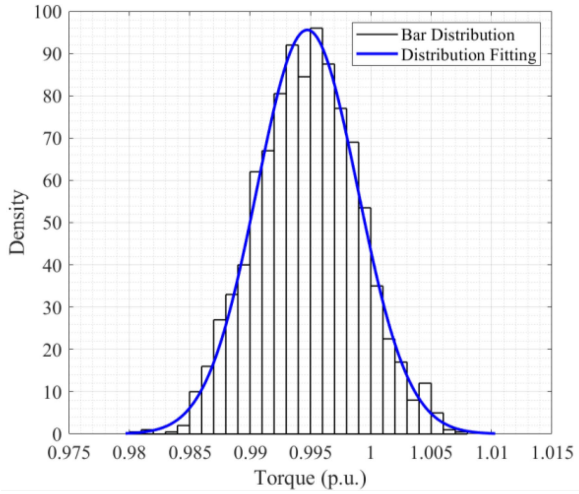

FIGURE 10. Probability density distribution of the torque obtained by Monte Carlo method.

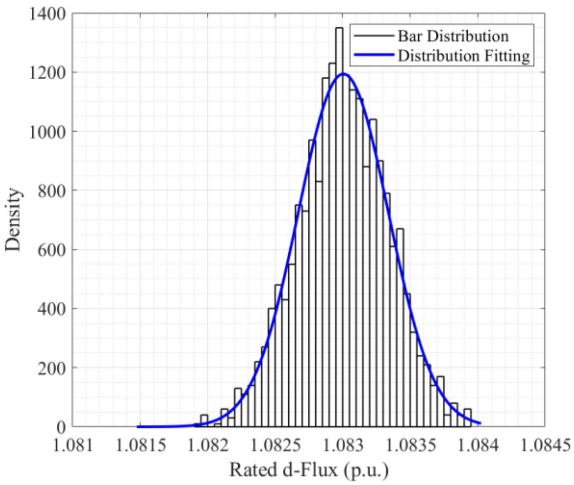

FIGURE 12. Probability density distribution of the *d*-axis flux obtained by Monte Carlo method.

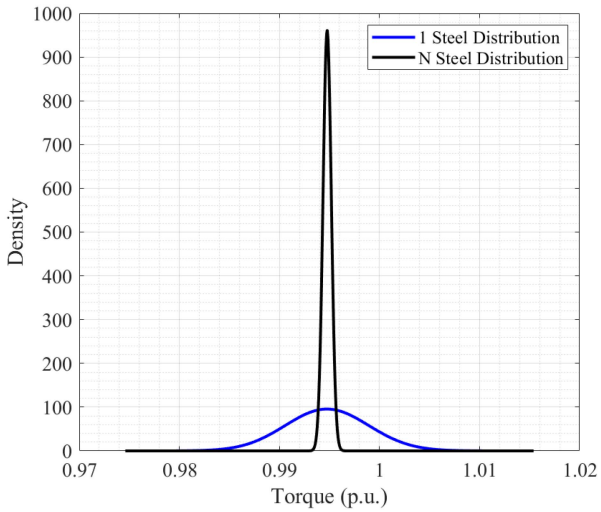

FIGURE 11. Comparison of the probability density distribution of the torque obtained by Monte Carlo method considering one and N electrical steels.

Still, this average torque is very close to the design value, and so significantly different from the one obtained in experiments, at nominal phase current. Therefore, the mechanical tolerances alone cannot justify the discrepancy between the FEA design and the experimental evidence.

A similar Monte Carlo analysis was conducted considering the *d*-axis flux at rated torque, as reported in Fig. 12. In this case, the standard deviation of the fitting normal distribution is lower than 0.15% of the rated flux, while its mean value is practically coincident with the rated value. Moreover, the deviation would further reduce by $\approx \sqrt{N}$ if a batch of N different laminations are considered. Therefore, the effect of manufacturing tolerances on the *d*-axis flux will be neglected in the following analyses.

The current method utilizes the *d*-axis flux linkage for model calibration. If needed, the Monte Carlo analysis could be easily extended to include the λ_q variations, particularly sensitive to mechanical tolerances in the case of high speed SynRel motors presenting radial ribs. For such cases, the effects of rib tolerances could be incorporated in the analysis without significantly increasing computational complexity.

B. EFFECT OF AIRGAP VARIATION

If the Monte Carlo analysis presented above permits the evaluation of the machine performance on varying simultaneously numerous parameters, a dedicated analysis was developed for the airgap thickness, because it is the geometrical variable that most affects the motor flux and torque. Since its value is typically small (0.5 mm in the motor under test), a slight variation within the manufacturing tolerance (typically 0.05 mm) can induce a relevant airgap variation, e.g., up to 10%, with a consequent drastic variation of the motor performance.

The effects of a linear variation of the airgap are analyzed, targeting the best fit with the measured torque and magnetization curve. In this case, the effects of N different laminations are neglected, and the analysis is carried out considering the same airgap for every lamination. The FEA simulation was executed several times on varying the airgap length, while the current was set on the MTPA, computed with FEA which is very close to the experimental one, with an amplitude of 36 Apk, i.e., the current required in experiments to obtain the nominal torque. This permitted a fair comparison with the measured torque and flux linkage.

The airgap was modified by varying the rotor's outer and the stator's inner diameter. This approach ensures a comprehensive evaluation of the effects of airgap variation on the machine's performance, as both components contribute to the effective airgap.

The computed torque and *d*-axis rated flux as a function of the airgap length is reported in Fig. 13. The results indicate that the airgap thickness that matches the measured torque (0.86 N·m, 1 p.u.) is 0.522 mm, which is +4.4% higher than

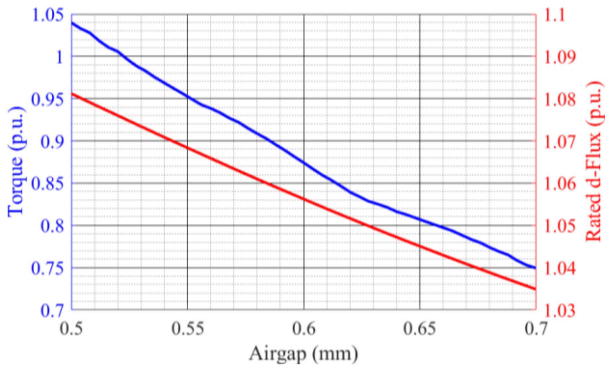

FIGURE 13. Output torque and rated d-flux as a function of the airgap length.

the design airgap, and within the expected mechanical tolerance. Conversely, the airgap length that matches the measured flux (1.058 p.u.) resulted in 0.592 mm, which is outside the realistic mechanical tolerance.

Overall, defining a correct airgap value to contemporarily guarantee an accurate torque and flux linkage representation in the FEA model is not possible. Therefore, another source of deviation from the simulation has been considered

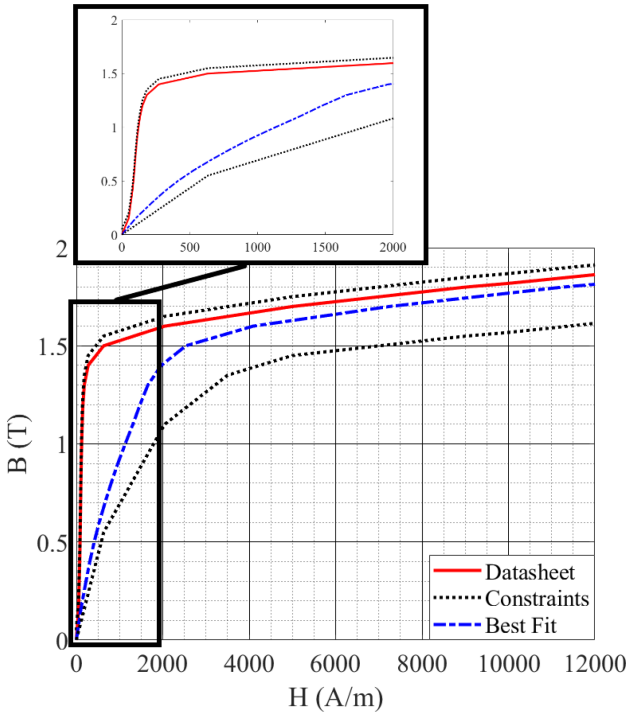

FIGURE 14. Comparison between BH curves from the datasheet, implemented constraints, and the one that correctly fits all the outputs of the motor.

C. MAGNETIC PROPERTIES DEGRADATION DUE TO THE MANUFACTURING PROCESS

The manufacturing process can introduce a degradation of the magnetic material in the cut area by either laser cutting or blanking [29]. The thickness of the damaged area and the entity of the degradation strongly depend on the adopted cutting technology and are hardly predicted at the design stage. This reduction is significant, with up to ten times reduction of the relative permeability in the linear region of the magnetic material, and particularly critical for small machines, where the degraded area is larger in percentage.

Traditionally, during the motor design stage, the B–H curve of the degraded material and its thickness are determined using the electrical steel datasheet, along with correction coefficients. These coefficients are typically derived empirically, based on experience or trial and error. In contrast, this article proposes a systematic method for determining the degraded B–H characteristic.

In order to find a correct match between the simulated and measured saturation curves and torque at the nominal current, a multiobjective optimization algorithm was adopted, computing the motor flux maps and torque on varying the shape of the magnetization curve. The goal is to find an equivalent degraded B–H characteristic to be uniformly applied to the full machine. The following constraints were imposed:

1) the magnetic permeability for every point is higher than μ_o (permeability of vacuum);
2) for a given magnetic field (H) the flux density (B) can be at most 0.1 T higher than the datasheet curve;
3) the maximum ratio between the absolute permeability in the datasheet and the simulated one, at every point, is lower than 10.

The result of this optimization is the deteriorated B–H curve reported in Fig. 14 (blue line), and compared with the datasheet saturation characteristic (red curve) and the optimization constraints (black lines). Such equivalent B–H curve is comparable, in terms of deviation from the datasheet, with the one measured in [29], where small degraded areas are considered.

An alternative method for calibrating the FEM model is to measure the B–H curve on cut lamination samples having different areas, thus inserting different saturation curves in different regions of the FEM model. An example of measured B–H curves is given in Fig. 15, where three laser-cut samples with degraded areas of 1, 2.5, and 5 mm were experimentally characterized. Based on these curves, in each element of the FEM model the B–H curve could be updated based on the thickness of the corresponding area. For example, the 5 mm curve could be adopted in the stator yoke, while for the teeth, having an average thickness of $\approx$2.1 mm, an average curve between the 1 and 2.5 mm cases should be set. Anyway, if this approach could provide acceptable results, several numerical issues arise when facing iron sections with different magnetization curves. Moreover, the algorithms for geometry optimization require a significantly higher computational time for converging, as it must include the possibility of modifying

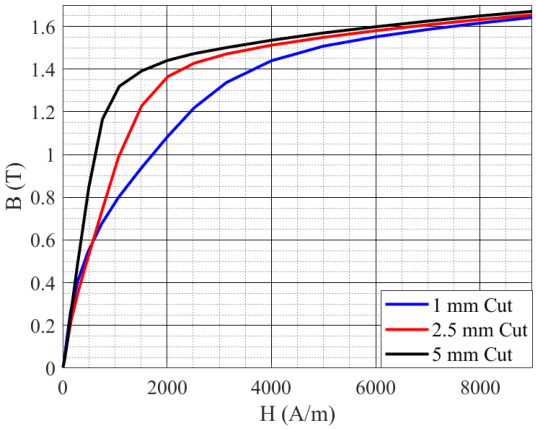

FIGURE 15. Comparison of B–H curves at different laser cut areas.

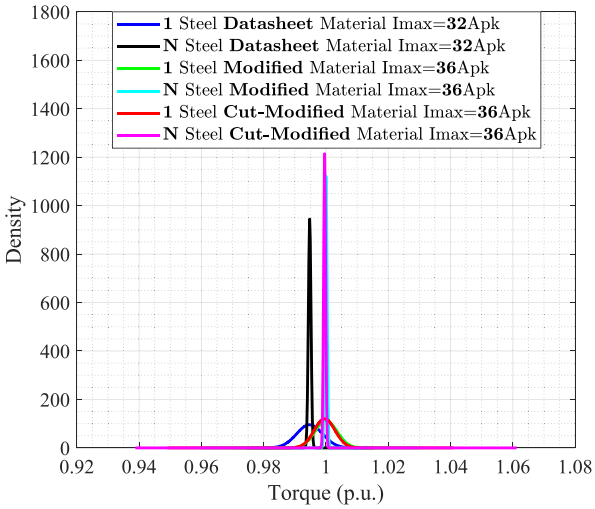

FIGURE 16. Comparison of the probability density distribution of the torque obtained by the Monte Carlo method considering one and *N* electrical steels for the datasheet material, the modified material obtained through multiobjective optimization and by imposing different BH curves in the different cut areas.

the B–H curve of selected elements at each iteration. Therefore, this approach was not further pursued.

The Monte Carlo analysis presented in Section IV-A was repeated, computing the motor torque on varying the geometrical tolerances, but imposing in the FEA model the equivalent B-H curve obtained in Fig. 14, i.e., optimized for best fitting the measured torque and flux linkage. The analysis was conducted with a phase current of 36 Apk, i.e., the current amplitude required for providing the rated torque in experiments. The obtained torque distribution is compared with the one in Fig. 11, i.e., with the nominal current of 32 Apk and the B–H curve from the steel datasheet. In both cases, a single steel lamination and a batch of N different laminations were considered. The results are reported in Fig. 16, showing again a Gaussian probability density of the computed torque.

As can be noted, the 36 Apk case produces ≈1.0 p.u. torque, confirming a perfect match between the experiments

TABLE 3. Final Comparison

OP	Current (Apk)	Standard FEM (N·m)	FEM with Modified Material (N·m)	Measured torque (N·m)
1	67.3	2.34	2.28	2.26
2	52.8	1.65	1.59	1.60
3	36.0	0.99	0.86	0.86
4	18.9	0.30	0.23	0.22

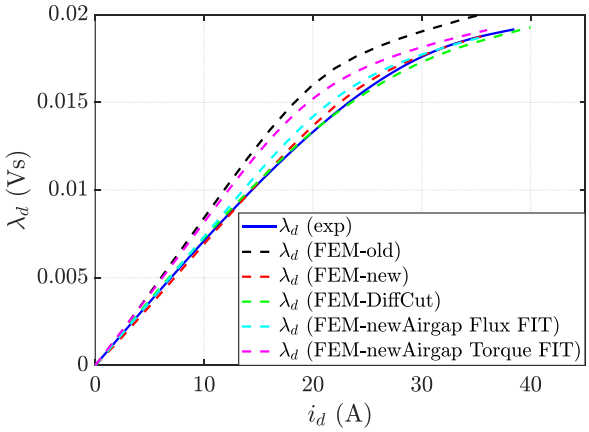

FIGURE 17. Comparison of $\lambda_d(i_d)$ characteristics; blue: experimental results, dashed lines: different FEA models.

and the ex-post calibrated FEA model, and practically canceling the 14.7% discrepancy between the measured torque and the estimation with the original model. Again, by considering N laminations the average torque is unchanged, but the standard deviation is significantly reduced.

As a further validation, the same Monte Carlo analysis was conducted when different material properties were applied to the different areas of the steel in the function of their size. Also with this approach, a correct match with the experimental results is obtained. Nevertheless, laser-cut material properties are often not available, so this study is used only for model verification.

D. BOTTOM LINE: PERFORMANCE COMPARISON AND CALIBRATED FLUX MAPS

Table 3 presents a summary of the torque results obtained using the experimental current values with the modified material obtained through multiobjective optimization and the datasheet material (Standard FEM). The results demonstrate that the new equivalent material effectively simulates the machine when considering manufacturing effects. Thus, the proposed method can be employed on the manufactured prototype to derive the modified BH curve for use in optimizations. The method's limitation lies in its applicability; it is valid under conditions where the motor dimensions, manufacturing process, and material are similar to the tested one.

Figs. 17 and 18 compare the flux maps obtained with the different calibration techniques proposed in this article and the experimental measures. The reported curves refer to the following.

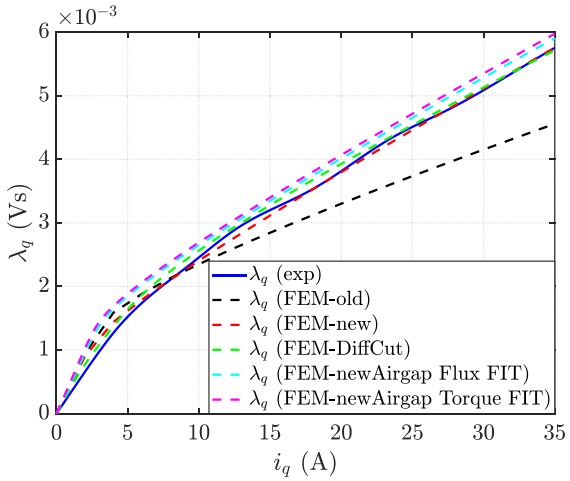

FIGURE 18. Comparison of $\lambda_q(i_q)$ characteristics; blue: experimental results, dashed lines: different FEA models.

1) Blue line: experimentally measured flux maps.
2) Black line: original FEA model, with the nominal B–H curve and without manufacturing tolerance.
3) Red line: ex-post calibrated model, with the computed B–H curve in the damaged cut area, assuming all the laminations to be equal (N=1).
4) Green line: ex-post calibrated model, with the computed B–H curve in the damaged cut area, assuming different batches of laminations (N=120).
5) Light blue line: nominal B–H curve without manufacturing tolerance on the stator and rotor edges, but with the airgap length that best fits the nominal flux linkage in d-axis.
6) Magenta line: nominal B–H curve without manufacturing tolerance on the stator and rotor edges, but with the airgap length that minimizes the error on the rated torque.
7) For a given magnetic field (H) the flux density (B) can be at most 0.1 T higher than the datasheet curve.

As can be noted, the ex-post calibrated model (red line), is well in accordance with the measurements. This result confirms that the proposed method permits to reach a good accuracy for the torque and flux computation compared to the experimental ones, by defining an equivalent material that considers the effect of laser cutting. Such new material can be used for further optimization in machines with similar dimensions.

In addition, a comparison in terms of losses is carried out to further validate the proposed model and is shown in Table 4.

The results demonstrate that the new model also correctly fits the losses, and so the efficiency computation of the machine in all operating points. The maximum loss error is reduced from 19% in OP3, initial model to 3% in OP4, final model.

TABLE 4. Motor Losses in the Initial Model, Calibrated Model, and Experimentally Measured

Operating Point	Joule Loss (W)	Rotational Loss (W) Mechanical + Core	Total Loss (W)	Torque (N·m)
1 (Initial)	186.54	30.57	217.11	2.26
1 (Final)	163.23	59.34	222.57	2.26
1 (Exp.)	163.13	60.1	223.23	2.26
2 (Initial)	94.23	33.88	128.11	1.60
2 (Final)	100.11	47.21	147.32	1.60
2 (Exp.)	100.49	45.5	145.99	1.60
3 (Initial)	38.15	22.1	60.25	0.86
3 (Final)	47.96	24.81	72.77	0.86
3 (Exp.)	48.15	25.8	73.95	0.86
4 (Initial)	12.3	19.91	32.21	0.22
4 (Final)	13.23	21.38	34.61	0.22
4 (Exp.)	13.16	22.41	35.57	0.22

V. FINAL REMARKS

A. CROSS-SATURATION

The proposed method calibrates and validates the FEA model considering manufacturing effects. While manufacturing influences the entire magnetic model, it has a stronger effect on self-axis magnetic saturation than on cross-saturation, which is less sensitive to tolerances. Therefore, this study focuses on the accuracy of self-saturation for FEA model calibration. Although including cross-saturation could improve the model accuracy, it would add computational complexity and require additional experimental tests. Therefore, cross-saturation is excluded from the calibration process to balance accuracy and complexity. Nevertheless, the accuracy of the magnetic model, including cross-saturation, is indirectly verified through torque accuracy evaluation.

B. ROTOR ECCENTRICITY

Recent literature [30], [31]; highlighted the importance of considering both eccentricity and dimensional tolerances when evaluating motor performance. Static and dynamic eccentricities can significantly alter the air gap distribution and generate unbalanced magnetic pull, affecting torque ripple and noise. However, dimensional variations due to manufacturing, even in the absence of eccentricity, are not negligible and must be carefully separated from fault indicators.

This study did not directly account for eccentricity, which is a common manufacturing defect in low-cost SynRel machines. However, in the motor under test, the eccentricity was minimal, as the machine was designed for a high maximum speeds, where an eventual eccentricity would lead to excessive noise and vibration. This was experimentally validated by repeating the flux map measurements from paper [21] at various rotor positions in 90° increments. The d-axis and q-axis saturation curves measured at different shaft positions showed negligible discrepancies, confirming that the impact of eccentricity on the motor's performance was limited. Nonetheless, eccentricity could be incorporated as an additional variable for statistical and sensitivity analyses, if necessary.

C. EXTENSION TO PMSMS

The adopted Monte Carlo simulations evaluate the impact of manufacturing tolerances, such as airgap variation and as a result a negligible effect under the specific conditions of synchronous reluctance machines have been found. However, this outcome is not necessarily generalizable to other topologies, such as PMSMs. In such cases, a more detailed tolerance analysis, including non-UUM effects, would be required to ensure accurate modeling and calibration.

VI. CONCLUSION

The mechanical tolerances and iron degradation due to the manufacturing process considerably affect the motor performance, especially for small machines. These effects are hardly evaluated analytically and are often included in the design optimization stage based on experience or by varying the design parameters through trial and error. This study provides a comprehensive procedure permitting a systematic ex-post calibration of the FEA model adopted for the design of a SynRel motor. The torque and flux linkage saturation characteristics in the dq axes are experimentally measured, revealing considerable discrepancies with respect to the FEA simulations. To correct this mismatch, the paper systematically investigates the influence of mechanical tolerances, airgap variations, and magnetic property degradation due to the manufacturing process.

The mechanical tolerances are corrected through a Monte Carlo analysis, while an optimization procedure determined an equivalent B–H curve to take into account the iron degradation in the cut areas. The analysis permits to obtain a refined FEA model that presents a negligible discrepancy with the measured torque and flux linkage characteristics. Such a refined FEA model is extremely useful for subsequent design optimizations of the machine or for the design of motors of similar size, avoiding the need to realize a preliminary prototype.

Although this study was conducted on a single prototype, the systematic methodology ensures that the results can be applied to similar machines. Additionally, the method's capability to estimate the degraded BH curve after manufacturing makes it applicable for designing new machines, as long as the manufacturing process remains consistent.

The analysis relies on a single test sample and does not incorporate a formal uncertainty quantification of the experimental measurements. Future work should include testing across multiple prototypes and incorporating confidence bounds into the calibration process, thereby further improving the robustness and generalizability of the proposed methodology.

Overall, this study contributes to a deeper understanding of the manufacturing-induced effects on SynRel motor performance permitting their inclusion into the motor design stage, when a machine with similar dimensions should be designed.

REFERENCES

[1] A. T. de Almeida, F. J. T. E. Ferreira, and G. Baoming, "Beyond induction motors—Technology trends to move up efficiency," *IEEE Trans. Ind. Appl.*, vol. 50, no. 3, pp. 2103–2114, May/Jun. 2014.

[2] R. Saidur, "A review on electrical motors energy use and energy savings," *Renewable Sustain. Energy Rev.*, vol. 14, no. 3, pp. 877–898, 2010.

[3] F. Oliveira and A. Ukil, "Comparative performance analysis of induction and synchronous reluctance motors in chiller systems for energy efficient buildings," *IEEE Trans. Ind. Informat.*, vol. 15, no. 8, pp. 4384–4393, Aug. 2019.

[4] K. Lang, A. Muetze, R. Bauer, and S. Pircher, "Comparison of induction and synchronous reluctance machine based actuators for elevated temperature environments," *IEEE Trans. Energy Convers.*, vol. 31, no. 3, pp. 1012–1022, Sep. 2016.

[5] G. Bramerdorfer, J. A. Tapia, J. J. Pyrhönen, and A. Cavagnino, "Modern electrical machine design optimization: Techniques, trends, and best practices," *IEEE Trans. Ind. Electron.*, vol. 65, no. 10, pp. 7672–7684, Oct. 2018.

[6] E. Carraro, M. Morandin, and N. Bianchi, "Optimization of a traction PMASR motor according to a given driving cycle," in *Proc. IEEE Transp. Electrific. Conf. Expo*, 2014, pp. 1–6.

[7] K. Diao, X. Sun, G. Lei, G. Bramerdorfer, Y. Guo, and J. Zhu, "System-level robust design optimization of a switched reluctance motor drive system considering multiple driving cycles," *IEEE Trans. Energy Convers.*, vol. 36, no. 1, pp. 348–357, Mar. 2021.

[8] B. Dianati, S. Kahourzade, and A. Mahmoudi, "Optimization of axial-flux induction motors for the application of electric vehicles considering driving cycles," *IEEE Trans. Energy Convers.*, vol. 35, no. 3, pp. 1522–1533, Sep. 2020.

[9] X. Sun, Z. Shi, Y. Cai, G. Lei, Y. Guo, and J. Zhu, "Driving-cycle-oriented design optimization of a permanent magnet hub motor drive system for a four-wheel-drive electric vehicle," *IEEE Trans. Transp. Electrific.*, vol. 6, no. 3, pp. 1115–1125, Sep. 2020.

[10] A. Credo, G. Fabri, M. Villani, and M. Popescu, "A robust design methodology for synchronous reluctance motors," *IEEE Trans. Energy Convers.*, vol. 35, no. 4, pp. 2095–2105, Dec. 2020.

[11] Y. Duan and D. M. Ionel, "A review of recent developments in electrical machine design optimization methods with a permanent-magnet synchronous motor benchmark study," *IEEE Trans. Ind. Appl.*, vol. 49, no. 3, pp. 1268–1275, May/Jun. 2013.

[12] C. Di, I. Petrov, J. J. Pyrhönen, and J. Chen, "Accelerating the time-stepping finite-element analysis of induction machines in transient-magnetic solutions," *IEEE Access*, vol. 7, pp. 122251–122260, 2019.

[13] Y. Yang, N. Bianchi, C. Zhang, X. Zhu, H. Liu, and S. Zhang, "A method for evaluating the worst-case cogging torque under manufacturing uncertainties," *IEEE Trans. Energy Convers.*, vol. 35, no. 4, pp. 1837–1848, Dec. 2020.

[14] D. Lee, A. Yoon, S. Sirimanna, S. Salon, and K. S. Haran, "Impact of manufacturing tolerances on a low-reactance slotless PM synchronous machine," *IEEE Trans. Energy Convers.*, vol. 35, no. 1, pp. 366–374, Mar. 2020.

[15] J. Kolb and K. Hameyer, "Sensitivity analysis of manufacturing tolerances in permanent magnet synchronous machines with stator segmentation," *IEEE Trans. Energy Convers.*, vol. 35, no. 4, pp. 2210–2221, Dec. 2020.

[16] W. Zhao, T. A. Lipo, and Y. Amara, "Robust design and tolerance analysis of permanent magnet machines using noise-based optimization and metamodeling," *IEEE Trans. Ind. Appl.*, vol. 56, no. 3, pp. 2861–2872, May/Jun. 2020, doi: 10.1109/TIA.2020.2967104.

[17] G. Bramerdorfer, "Quantifying the impact of tolerance-affected parameters on the performance of permanent magnet synchronous machines," *IEEE Trans. Energy Convers.*, vol. 35, no. 4, pp. 2170–2180, Dec. 2020, doi: 10.1109/TEC.2020.2997391.

[18] J. Kolb and K. Hameyer, "Assessment of uncertainties and tolerances in electrical machines," *IEEE Trans. Magn.*, vol. 60, no. 3, Mar. 2024, Art. no. 8100506, doi: 10.1109/TMAG.2023.3317494.

[19] M. Bali and A. Muetze, "The degradation depth of non-grain oriented electrical steel sheets of electric machines due to mechanical and laser cutting: A state-of-the-art review," *IEEE Trans. Ind. Appl.*, vol. 55, no. 1, pp. 366–375, Jan./Feb. 2019.

[20] S. Ferrari and G. Pellegrino, "FEA-augmented design equations for synchronous reluctance machines," in *Proc. IEEE Energy Convers. Congr. Expo.*, 2018, pp. 5395–5402.

[21] N. Bianchi, E. Fornasiero, M. Ferrari, and M. Castiello, "Experimental comparison of PM assisted synchronous reluctance motors," in *Proc. IEEE Energy Convers. Congr. Expo.*, 2014, pp. 4499–4506.
[22] A. Varatharajan, P. Pescetto, and G. Pellegrino, "Sensorless synchronous reluctance motor drives: A full-speed scheme using finite-control-set MPC in a projection vector framework," *IEEE Trans. Ind. Appl.*, vol. 56, no. 4, pp. 3809–3818, Jul./Aug. 2020.
[23] J. Yoo, J. Lee, and S.-K. Sul, "Analysis of instability in torque control of sensorless PMSM drives in flux weakening region," *IEEE Trans. Power Electron.*, vol. 36, no. 9, pp. 10815–10826, Sep. 2021.
[24] M. Hinkkanen, P. Pescetto, E. Mölsä, S. E. Saarakkala, G. Pellegrino, and R. Bojoi, "Sensorless self-commissioning of synchronous reluctance motors at standstill without rotor locking," *IEEE Trans. Ind. Appl.*, vol. 53, no. 3, pp. 2120–2129, May/Jun. 2017.
[25] L. Peretti, P. Sandulescu, and G. Zanuso, "Self-commissioning of flux linkage curves of synchronous reluctance machines in quasi-standstill condition," *IET Elect. Power Appl.*, vol. 9, no. 9, pp. 642–651, Nov. 2015.
[26] A. Credo and P. Pescetto, "Design optimization of a synchronous reluctance motor based on operating cycle," in *Proc. Int. Conf. Elect. Machines*, 2020, pp. 2486–2492.
[27] R. R. Mpghaddam, "Synchronous reluctance machine (SynRM) in variable speed drives (VSD) applications," Ph.D dissertation, The Royal Inst. Technol. (KTH), Stockholm, Sweden, 2011.
[28] M. Pohl and D. Gerling, "Analytical model of synchronous reluctance machines with Zhukovski barriers," in *Proc. XIII Int. Conf. Elect. Mach.*, 2018, pp. 91–96.
[29] A. Credo, I. Petrov, J. Pyrhönen, and M. Villani, "Impact of manufacturing stresses on multiple-rib synchronous reluctance motor performance," *IEEE Trans. Ind. Appl.*, vol. 59, no. 2, pp. 1253–1262, Mar./Apr. 2023.
[30] B. Galfarsoro, I. Zamora, A. Iraolagoitia, and E. Torres, "Analysis of rotor eccentricity and geometrical tolerances in PMSMs: Fault detection versus manufacturing effects," *IEEE Trans. Ind. Electron.*, vol. 69, no. 8, pp. 7720–7729, Aug. 2022, doi: 10.1109/TIE.2021.3105805.
[31] B. Galfarsoro, I. Zamora, A. Iraolagoitia, and E. Torres, "Assessment of the combined effect of eccentricity and mechanical tolerances in electric machines through harmonic signature analysis," *Energies*, vol. 15, no. 7, Apr. 2022, Art. no. 2589, doi: 10.3390/en15072589.

ANDREA CREDO (Member, IEEE) received the B.Sc. and M.Sc. degrees in electrical engineering in 2015 and 2017, respectively, from the University of L'Aquila, L'Aquila, Italy, where he has been working toward the Ph.D. (Cum Laudem) degree in 2021 from the same university, with a focus on the design and modeling of synchronous reluctance motors for automotive applications since 2017.

He is an Assistant Professor with the University of L'Aquila. In 2022, he was a Research Fellow with the Lappeenranta University of Technology, Finland. He is currently a Research Fellow with the University of L'Aquila. His research interests include the design and control of synchronous reluctance motors.

Dr. Credo was the recipient of the ICEM Jorma Luomi Student Forum Award during the ICEM 2020 in Gothenburg, Sweden (Virtual Conference).

PAOLO PESCETTO (Member, IEEE) received the Ph.D. (Hons.) degree in design and senorless control of high-anisotropy synchronous motor drives, including self-commissioning techniques and advanced position estimation algorithms from Politecnico di Torino, Turin, Italy, in 2019.

He is an Assistant Professor with Politecnico di Torino. Since fall 2019, he has been working as a Researcher and tenure-track Lecturer with the Energy Department, Politecnico di Torino. He is a member of the Power Electronics Innovation Center (PEIC) of Politecnico di Torino. In 2014, he was an Erasmus Student with the Norwegian University of Science and Technology, Trondheim, Norway. He authored or coauthored 50+ scientific works, with more than 15 IEEE journal papers and five patents. Since 2022, he has been the Vice Chair of the IEEE IA/IE/PEL North Italy Joint Chapter. His main research interests include synchronous motor drives, sensorless control, self-commissioning techniques, thermal models, and integrated battery chargers for EVs.

Dr. Pescetto has been an Associate Editor of IEEE TRANSACTIONS ON TRANSPORTATION ELECTRIFICATION since 2024. He was the recipient of five IEEE paper awards and two IEEE Ph.D. thesis awards.